

1 **Charged nanograins in the Enceladus plume**

2

3 T. W. Hill,<sup>1</sup> M. F. Thomsen,<sup>2</sup> R. L. Tokar,<sup>2</sup> A. J. Coates,<sup>3</sup> G. R. Lewis,<sup>3</sup> D. T. Young,<sup>4</sup> F. J.

4 Crary,<sup>4</sup> R. A. Baragiola,<sup>5</sup> R. E. Johnson,<sup>5</sup> Y. Dong,<sup>1</sup> R. J. Wilson,<sup>6</sup> G. H. Jones,<sup>3</sup> J.-E. Wahlund,<sup>7</sup>

5 D. G. Mitchell,<sup>8</sup> and M. Horányi<sup>6</sup>

6

7 \_\_\_\_\_

8 <sup>1</sup>Rice University, Houston, Texas, USA

9 <sup>2</sup>Los Alamos National Laboratory, Los Alamos, New Mexico, USA

10 <sup>3</sup>Mullard Space Science Laboratory, University College London, Dorking, Surrey, UK

11 <sup>4</sup>Southwest Research Institute, San Antonio, Texas, USA

12 <sup>5</sup>University of Virginia, Charlottesville, Virginia, USA

13 <sup>6</sup>University of Colorado, Boulder, Colorado, USA

14 <sup>7</sup>Swedish Institute of Space Physics, Uppsala, Sweden

15 <sup>8</sup>Johns Hopkins University, Laurel, Maryland, USA

16

17

18

19 Submitted to *Journal of Geophysical Research*, 1 October 2011

20

20 **Abstract:**

21

22       There have been three Cassini encounters with the south-pole eruptive plume of Enceladus  
23 for which the Cassini Plasma Spectrometer (CAPS) had viewing in the spacecraft ram direction.  
24 In each case, CAPS detected a cold dense population of heavy charged particles having mass-to-  
25 charge ( $m/q$ ) ratios up to the maximum detectable by CAPS ( $\sim 10^4$  amu/e). These particles are  
26 interpreted as singly charged nanometer-sized water-ice grains. Although they are detected with  
27 both negative and positive net charges, the former greatly outnumber the latter, at least in the  $m/q$   
28 range accessible to CAPS. On the most distant available encounter (E3, March 2008) we derive  
29 a net (negative) charge density of up to  $\sim 2600$  e/cm<sup>3</sup> for nanograins, far exceeding the ambient  
30 plasma number density, but less than the net (positive) charge density inferred from the RPWS  
31 Langmuir probe data during the same plume encounter. Comparison of the CAPS data from the  
32 three available encounters is consistent with the idea that the nanograins leave the surface vents  
33 largely uncharged, but become increasingly negatively charged by plasma electron impact as  
34 they move farther from the satellite. These nanograins provide a potentially potent source of  
35 magnetospheric plasma and E-ring material.

36

37 **Index terms:** 2756, 5737 (planetary magnetospheres), 6280 (Saturnian satellites)

38 **Introduction**

39

40 Enceladus is a small icy satellite (radius  $R_E \approx 252$  km) that orbits Saturn at a distance of  
41 about  $3.95 R_S$  (Saturn's equatorial radius  $R_S \approx 60,300$  km). Despite its small size, Enceladus is  
42 geologically active, for reasons that are not established. Evidence for this activity includes linear  
43 “tiger stripe” features at high southern latitudes that are much warmer than the surrounding  
44 surface (Spencer et al., 2006) and associated eruptive jets or plumes that extend several  $R_E$  into  
45 space and are made visible by forward scattering of sunlight by micron-size dust (Porco et al.,  
46 2006). In addition to the visible micron-size dust, these plumes also contain copious amounts of  
47 neutral-water vapor (Hansen et al., 2006; Waite et al., 2006), negative water-cluster molecular  
48 ions (Coates et al., 2009), positive water-group ions (Tokar et al., 2009), charged nanometer-  
49 sized grains (Jones et al., 2009), and cold dense plasma (Shafiq et al., 2011). The charged  
50 nanometer-size grains ("nanograins") are the subject of this paper.

51

52 The Cassini spacecraft has made several targeted encounters with the Enceladus plume. Of  
53 these, three provided ram pointing (in the direction of spacecraft motion) for the Cassini Plasma  
54 Spectrometer (CAPS) instrument, encounters E3 (12 Mar 2008), E5 (9 Oct 2008), and E7 (2 Nov  
55 2009); see Figure 1. All three passed very close to the plume axis ( $\approx$  the south polar axis of  
56 Enceladus). Ram pointing is a requirement for CAPS detection of these cold, heavy charged  
57 grains. Here we present our analysis of CAPS nanograin observations during the E3, E5, and E7  
58 encounters and our expectations for future encounters.

59

60

## 60 **Observations**

61

62 CAPS contains three detector systems, an Electron Spectrometer (ELS), an Ion Mass  
63 Spectrometer (IMS), and an Ion Beam Spectrometer (IBS). The ELS provides electrostatic  
64 energy-per-charge ( $E/q$ ) analysis of electrons in the range  $0.7 - 28,800$  eV/e, and any other  
65 negatively-charged particles that fall in the same  $E/q$  range, e.g., the cold heavy negative ions  
66 discovered in the ionosphere of Titan (Coates et al., 2007) and in the Enceladus plume (Coates et  
67 al., 2009) that are boosted into the ELS energy range by the spacecraft ram velocity. The IMS  
68 provides electrostatic  $E/q$  analysis of positive ions in the range  $1 - 34,700$  eV/e, and also  
69 includes a time-of-flight (TOF) system for composition ( $m/q$ ) analysis. Both ELS and IMS have  
70 fan-shaped fields of view spanning  $5^\circ \times 160^\circ$  (ELS) and  $8^\circ \times 160^\circ$  (IMS), divided into eight  
71 contiguous angular sectors of  $5^\circ \times 20^\circ$  (ELS) and  $8^\circ \times 20^\circ$  (IMS). The IBS detects ions in a  
72 specifiable subset of the IMS  $E/q$  range, but has a much narrower field of view designed to  
73 resolve highly collimated beams like the solar wind. Because Cassini is a non-spinning  
74 spacecraft, the detectors are mounted on an actuator platform that, when activated, provides a  
75  $180^\circ$  sweep in the azimuthal direction, but the actuator was deactivated during the three  
76 encounters discussed here in order to provide steady viewing of the spacecraft ram direction,  
77 which appears in anode 5 (the fifth of the eight angular sectors) on the E3 and E5 encounters,  
78 and in anode 4 on E7. In this paper we utilize data from ELS and IMS. Accumulation times  
79 were insufficient for TOF analysis, and IBS signals, when available, were consistent with the  
80 corresponding IMS signals. For further description of CAPS see Young et al. (2004).

81

82 Figure 2 shows counting-rate spectrograms from ELS (top panel) and IMS (bottom panel) for  
83 a five-minute interval surrounding the E3 encounter on 12 Mar 2008. Figure 3 shows the same  
84 thing for the E5 encounter on 9 Oct 2008. The counting rate is roughly proportional to particle  
85 energy flux. The ELS counting rate is from anode 5, one of the two angular sectors (4 and 5)  
86 that border on the spacecraft ram direction, while the IMS counting rate is summed over all  
87 anodes to enhance the signal-to-noise ratio, but is dominated by the anodes closest to the ram  
88 direction for the feature of interest here. For both encounters, the nanograin signature occurs  
89 near the top of the CAPS  $E/q$  range, above a few 100 eV/e for ELS and a few 1000 eV/e for  
90 IMS. The lower- $E/q$  signals are from ambient plasma and locally produced ions discussed by  
91 Coates et al. (2009) and Tokar et al. (2009). The nanograin populations, discussed by Jones et al.  
92 (2009) and Coates et al. (2010), obviously extend well beyond the upper limit of the CAPS  $E/q$   
93 ranges for both ELS and IMS. The nanograin signature in the IMS spectrogram is similar in  
94 shape to that in the ELS spectrogram but is shifted higher in energy and peaks later in time.

95  
96 Figure 4 shows spectra of counting rates versus  $E/q$  for negative (ELS) and positive (IMS)  
97 particles on the E3 encounter, at times near the respective peaks of the nanograin flux. Figure 5  
98 shows the same thing for the E5 encounter. The upper horizontal scales show the corresponding  
99  $m/q$  range in units of H<sub>2</sub>O molecular masses per elementary charge (18 amu/e), assuming  $E =$   
100  $mv^2/2$  where  $v$  = spacecraft speed relative to Enceladus (see below). These spectra are vertical  
101 2D slices through the 3D spectrograms of Figures 2 and 3, respectively. For the E3 encounter  
102 (Figure 4), the negative water-cluster ions at discrete  $m/q$  values described by Coates et al.  
103 (2009) are clearly evident in the ELS spectrum; the positive molecular pick-up ions described by

104 Tokar et al. (2009) are not evident in the IMS spectrum because they peaked 12 sec (= 173 km)  
105 earlier.

106

107 Comparison of counting rates between adjacent angular sectors (not shown here) shows  
108 conclusively that the nanograins comprise highly collimated beams in the spacecraft reference  
109 frame, and hence represent cold populations that are almost at rest with respect to Enceladus  
110 (Jones et al., 2009; Tokar et al., 2009). The observed shape of the  $E/q$  distribution is due almost  
111 entirely to the spacecraft ram velocity. (The spacecraft potential relative to the plasma is  
112 assumed here to be negligible, a perfectly adequate assumption for the signatures at  $E/q > \sim 100$   
113 eV/e considered here.) The encounter speeds relative to Enceladus were  $v = 14.4, 17.7,$  and  $7.7$   
114 km/s for E3, E5, and E7 respectively. These encounter speeds imply  $E/m$  conversion factors  $v^2/2$   
115 = 1.1, 1.6, and 0.31 eV/amu respectively. There is a small but unknown correction due to the  
116 beam speed relative to Enceladus, which is not measured. The fact that the beams appear in the  
117 nominal ram direction but not in adjacent sectors indicates that this correction, if known, would  
118 be small.

119

## 120 **Density distribution**

121

122 If the beam were to uniformly fill one particular angular sector of the instrument, it would be  
123 straightforward to compute the partial number density within each  $E/q$  channel (or, equivalently,  
124 each  $m/q$  channel) simply by multiplying the differential number flux in that sector by  $v\Delta\Omega/2$   
125 where  $\Delta\Omega$  is the solid angle subtended by that sector. Summing these contributions over  $E/q$

126 channels would then provide an estimate of the total number density of particles within the  
127 CAPS  $E/q$  range that are visible in that angular sector.

128

129 However, as noted above, comparison of adjacent sectors indicates that the beam's angular  
130 width is less than, and possibly much less than, the angular width of a sector, so this approach  
131 would yield only an upper limit, and possibly not a very close upper limit, to the density. In this  
132 situation, a more accurate density determination is provided by the cold monoenergetic beam  
133 assumption employed by Coates et al. (2007) in their analysis of heavy negative ions in the  
134 atmosphere of Titan:

135

$$136 \quad C(E/q) = \epsilon n(E/q) v A \quad (1)$$

137

138 where  $C(E/q)$  is the observed counting rate per  $E/q$  channel in the angular sector that includes the  
139 ram direction,  $\epsilon$  is the detector counting efficiency (counts/particle),  $n(E/q)$  is the number density  
140 of those particles that occupy the given  $E/q$  channel,  $v$  is the ram speed, and  $A$  is the collecting  
141 area per angular sector. For the collecting area we take  $A = 0.33 \text{ cm}^2$  both for ELS and IMS,  
142 which is subject to an uncertainty of perhaps a few tens of percent owing to the nonlinear  
143 response to a monoenergetic beam as a function of its location within the field of view of a given  
144 angular sector. An even larger uncertainty may apply to the counting efficiency  $\epsilon$ , due primarily  
145 to uncertainty in the response of the micro-channel-plate detectors to slow heavy ions ( $\gg 100$   
146 amu/e). For ELS we provisionally assume an efficiency  $\epsilon(-) \sim 0.05$  on the basis of laboratory  
147 measurements and modeling calculations presented by Fraser (2002). This is uncertain by  
148 perhaps a factor  $\sim 2 - 3$ , and may well depend on  $E/q$ , though it is taken here as a constant,

149 lacking evidence to the contrary. For IMS we assume  $\epsilon(+)\approx 1$ , with a smaller uncertainty,  
150 because the impact of such massive particles on the thin ( $0.5\ \mu\text{g}/\text{cm}^2$ ) carbon foils (present in  
151 IMS but absent in ELS) virtually assures the registration of one (and only one) start pulse and  
152 one end pulse in the counting circuit.

153

154 Using these instrument parameters in (1) we derive the number density per unit mass  $dn/dm$   
155 of charged nanograins shown in Figures 6 (for E3) and 7 (for E5) at times near, but not at, the  
156 peak nanograin flux. We assume here that the charge per grain is  $\pm 1\ e$ , as discussed further  
157 below. In these plots we include only those particles that are plausibly identifiable as nanograins  
158 in Figures 2 and 3 while excluding ambient plasma, locally produced molecular and cluster ions,  
159 and background counts. This provides the somewhat arbitrary but operationally sufficient  
160 criteria  $m/q > 200\ \text{amu}/e$  for ELS and  $m/q > 1700\ \text{amu}/e$  for IMS. Note that these spectra appear  
161 to have reached their peaks near the top end of the CAPS  $E/q$  range. Because we cannot  
162 determine the shape of the  $dn/dm$  spectra above the top of our  $E/q$  range, all we can say is that  
163 our measured charged nanograin densities are certainly less than, and possibly much less than,  
164 the total charged nanograin densities.

165

166 Integrating over these  $dn/dm$  spectra gives the total charged nanograin density within the  
167 CAPS  $E/q$  range for each spectrum. Repeating this for each of 120 such spectra obtained during  
168 each encounter interval, we obtain the time series  $n(t)$  as shown in Figure 8. Maximum values  
169 are  $n(-)\sim 2600/\text{cm}^3$  at 19:06:41 UT on E3 (top panel) and  $\sim 760/\text{cm}^3$  at 19:07:03 UT on E5  
170 (bottom panel), and  $n(+)\sim 0.9/\text{cm}^3$  (19:06:59 UT on E3) and  $\sim 0.4/\text{cm}^3$  (19:07:10 UT on E5).  
171 Notwithstanding the considerable uncertainties in the counting efficiencies noted after equation

172 (1) above, there is no escaping the fact that the negative nanograins vastly outnumber the  
173 positive ones. Given the fact that each nanograin must carry at least  $\pm 1$  excess elementary  
174 charge in order to be detected by CAPS, it is also clear that the (net negative) charge density  
175 carried by such grains locally exceeds those (both positive and negative, presumably balanced)  
176 carried by the ambient plasma ( $\sim 100/\text{cm}^3$ ) in the Enceladus torus (Thomsen et al., 2010). It is,  
177 however, considerably less than the (oppositely unbalanced) peak charge density of the localized  
178 plume plasma during E3 as reported by Shafiq et al. (2011) and Morooka et al. (2011) on the  
179 basis of Radio and Plasma Wave Science – Langmuir Probe (RPWS–LP) data.

180

181 For the later E7 encounter (2 Nov 2009) we do not have clear-cut results comparable to  
182 Figures 2 – 8 shown above for E3 and E5, although E7 passed similarly close to the south polar  
183 axis at a distance much closer to the surface source, with the required CAPS ram pointing. (The  
184 south polar axis crossings of E3, E5, and E7 occurred at distances of 2.6, 1.3, and 0.4  $R_E$  from  
185 the south-pole surface point, respectively, as indicated in Figures 1 and 9.) On E7, a positive  
186 nanograin signal was not detected by IMS. A negative nanograin signal was detected by ELS,  
187 but with a much lower signal-to-noise ratio than on the other two encounters. It was possible to  
188 calculate a total nanograin density profile from (1) analogous to Figure 8 which, although noisy,  
189 showed a distinct peak with maximum density of  $1.4/\text{cm}^3$  at 07:41:51 UT, very near the closest  
190 approach to the south polar axis. The qualitative appearance of the E7 ELS spectrogram was as  
191 if the ELS signatures in Figures 2 and 3 were displaced vertically upward, almost but not quite  
192 past the top of the ELS  $E/q$  range.

193

194 Including this ELS E7 data point, we show in Figure 9 a summary of the charged nanograin  
195 observations on the three encounters for which such measurements were enabled by the CAPS  
196 viewing direction. The ordinate is the maximum density recorded during each encounter, and the  
197 abscissa is the corresponding distance from the surface of Enceladus (not from the center of  
198 Enceladus) along the south polar axis. Also shown for comparison is the  $1/r^2$  dependence that  
199 would be expected for a flux-conserving expansion from a time-independent source. There is, of  
200 course, no reason to expect that the source is time-independent over intervals of several months,  
201 but it is worth noting that the neutral water-vapor component of the plume, as measured by the  
202 Cassini Ion and Neutral Mass Spectrometer (INMS), was found to vary only by factors  $\sim 2$   
203 among these three encounters (Dong et al., 2011) when extrapolated back to the source. By  
204 comparison, the neutral gas cloud model of Smith et al. (2010), integrated in time over several  
205 months, indicates a factor  $\sim 4$  increase of the total source rate during the 7-month interval  
206 between E3 and E5.

207

## 208 **Particle size**

209

210 The conversion from observed  $E/q$  to intrinsic  $m/q$  is straightforward and probably correct,  
211 given that the particle speed relative to the spacecraft is dominated by the (known) spacecraft  
212 speed relative to Enceladus. To infer the particle mass we must assume something about its  
213 charge, and to convert mass to size we must further assume something about its density and  
214 structure.

215

216 We assume that the bulk of the nanograins have either  $q = 0$  (hence undetectable by CAPS),  
217 or  $q = -1 e$  (a single excess electron, hence detectable by ELS for sufficiently small  $m$ ). For  
218 justification of this assumption please see the discussion in the following section. To convert  
219 mass to size, let us adopt the conventional assumption of compact spheres having the density and  
220 composition of water ice. The bulk water composition is, in fact, confirmed by analysis of grain  
221 impacts on the INMS instrument (Waite et al., 2009, Supplemental Information). The  
222 assumption of compact spheres is probably incorrect, but provides a useful lower limit for the  
223 particle size corresponding to a given particle mass. The conversion from mass  $m$  to radius  $a$  is  
224 then

$$226 \quad \frac{a}{1 \text{ nm}} > \left( \frac{m}{2500 \text{ amu}} \right)^{1/3} \quad (2)$$

227  
228 which represents a lower limit because a complex grain structure would be less dense than a  
229 compact sphere. The lower limit is, however, probably of the appropriate order of magnitude  
230 because it depends only on the 1/3 power of the density.

231  
232 As noted above, the encounter speeds were 14.4, 17.7, and 7.7 km/s, respectively, for the E3,  
233 E5, and E7 encounters. The top of the ELS  $E/q$  range (30 keV/e) then corresponds to masses up  
234 to 27000, 19000, and 97000 amu respectively (1500, 950, and 4900 H<sub>2</sub>O molecular masses), or  
235 radii up to 2.2, 2.0, and 3.4 nm respectively. (Masses rounded to the nearest 1000 amu.) Thus,  
236 the designation "nanograin" is more appropriate than the more conventional "sub-micron grain"  
237 for the charged grains detectable by CAPS.

238

239 **Implications for charging mechanisms**

240

241 Following the E3 and E5 encounters it was suggested (Jones et al., 2009) that frictional  
242 (triboelectric) charging within the surface vents was a possible mechanism for charging the  
243 nanograins. Triboelectric charging can produce both negative and positive grains in comparable  
244 numbers, with negative charges favored for smaller particles and positive for larger ones. *In situ*  
245 plasma charging, by contrast, strongly favors negative grains for all particle sizes because the  
246 ambient electron flux typically exceeds the positive ion flux by a large factor.

247

248 The analysis shown here strongly favors the *in situ* charging hypothesis for three reasons: (1)  
249 the negative grains do indeed greatly outnumber the positive ones (Figures 4 – 8 above), as  
250 expected for *in situ* plasma charging; (2) the trend shown in Figure 9 strongly suggests that the  
251 nanograins leave Enceladus largely uncharged, thus explaining their relatively weak signal in  
252 ELS and the absence of a signal in IMS on the much closer E7 encounter; and (3) electron-  
253 impact charging becomes much faster, and hence more viable, in light of the very dense plume  
254 plasma reported by Shafiq et al. (2011) and Morooka et al. (2011) on the basis of RPWS–LP  
255 data.

256

257 The density peak of the LP plasma ions (Figure 2 of Shafiq et al.) closely resembles, in  
258 location and shape, the density peak of the negative nanograins shown in the top panel of Figure  
259 8 above for the same encounter. Moreover, the LP plasma data indicate a strong charge density  
260 imbalance of the opposite sense to that indicated by the nanograin data:  $n(+)$   $\gg$   $n(-)$  for the  
261 plasma and vice-versa for the nanograins. Taken in isolation, either of these results would be

262 suspect because charge quasi-neutrality is enforced quite rigorously on spatial scales  $\gg$  the  
263 Debye length and time scales  $\gg$  the electron plasma period, both of which conditions are easily  
264 satisfied on the spatial and temporal scales of these measurements. Taken together, however, the  
265 two results are quite compatible; indeed, they require each other for consistency. In fact, the  
266 presence of sub-micron-sized grains in the plume has already been inferred (Farrell et al., 2009,  
267 2010; Wahlund et al., 2009; Shafiq et al., 2011; Marooka et al., 2011) as needed to explain the  
268 LP result  $n(+) \gg n(-)$ . It seems quite plausible that the nanograins carry most of the negative  
269 charge in the dusty plasma environment of the plume. The numbers do not match in detail:  $n(+)$   
270  $- n(-) \sim 10^4/\text{cm}^3$  for the LP plume plasma versus  $n(-) - n(+) \sim 10^3/\text{cm}^3$  for the nanograins near  
271 the respective peaks. However, we have already noted above that CAPS can detect only a  
272 fraction (perhaps a small fraction) of the charged nanograins because they extend well off the top  
273 of the CAPS  $E/q$  range.

274

275 We suggest that the most likely (nonzero) charge on each nanograin is  $q = -1 e$  (a single  
276 excess electron), for three independent reasons. First, a purely statistical reason: if the  
277 probability of acquiring a single excess electron through inelastic collisions is  $p < 1$ , then the  
278 probability of acquiring  $n$  excess electrons, even ignoring electrostatic repulsion, is  $p^n < p$ .  
279 Secondly, an empirical reason: if there were a significant abundance of multiply-charged grains  
280 one would expect, for each singly-charged  $m/q$  peak, a series of ghost peaks at integral fractions  
281 ( $1/2$ ,  $1/3$ , etc.) of the main  $m/q$  peak value, and these are not observed. This argument is  
282 particularly compelling for the well-resolved  $m/q$  peaks of the smaller negative cluster ions  
283 evident in Figure 4 (top panel) below  $\sim 20$   $\text{H}_2\text{O}$  molecular masses per elementary charge.

284

285 The third reason is physical: each electron attached to a grain makes it less likely that another  
 286 will be attached, because of electrostatic repulsion. The extreme case of this is the steady-state  
 287 equilibrium grain potential, where the grain is sufficiently charged to repel the entire thermal  
 288 electron flux (minus the much smaller positive ion flux) by Debye shielding. For a Maxwellian  
 289 electron velocity distribution in an  $O^+$ -dominated plasma this equilibrium potential is

290

$$291 \quad \phi_{eq} \approx -3.6kT_e/e \sim -10V \quad (3)$$

292

293 independent of grain size (e.g., Horányi, 1996), corresponding to an equilibrium grain charge

294

$$295 \quad q_{eq} = 4\pi\epsilon_0 a \phi_{eq} \sim -7e (a/1 \text{ nm}) \quad (4)$$

296

297 This is too large to be relevant to limiting the grain charge to  $-1 e$ . But there is a more stringent  
 298 upper limit imposed by field emission, where the electrostatic repulsion potential between two  
 299 neighboring excess electrons exceeds their work function in the material of the grain. For  
 300 compact spherical ice grains the field emission limiting potential is

301

$$302 \quad \phi_{fe} \approx -1V (a/1 \text{ nm}) \quad (5)$$

303

304 (Mendis and Axford, 1974), corresponding to a limiting grain charge

305

$$306 \quad q_{fe} \sim -0.7e (a/1 \text{ nm})^2 \quad (6)$$

307

308 which is clearly relevant. This limit will be even smaller if the grain is neither compact nor  
 309 spherical, as seems likely. We propose that the effective limit for nanometer-sized grains is  $-1 e$ ,  
 310 because a single excess electron cannot repel itself.

311

312 Any one of the above three arguments taken alone might be considered less than compelling.  
 313 Taken together, however, they strongly support the conclusion that  $q = -1 e$  is the most likely  
 314 charge state, if not the only stable charge state, of the nanograins measured by CAPS on these  
 315 three encounters. It is worth noting that the field-emission limit (6) is less than the Debye-  
 316 shielding limit (4) for grain radii less than  $\sim 10$  nm, which includes all grains detectable by CAPS  
 317 on these encounters.

318

319 Finally, let us estimate the time and space scales relevant to grain charging by electron  
 320 attachment in the plume environment. A spherical grain with radius  $a$  has a surface area  $S =$   
 321  $4\pi a^2$  available to intercept an isotropic electron flux, assuming unit sticking efficiency. (The  
 322 sticking efficiency may well be  $< 1$  or even  $\ll 1$ , but this does not affect the comparisons below if  
 323 the sticking efficiency is independent of the grain size and of distance from Enceladus.) The  
 324 plasma has a thermal electron flux  $F_e = n_e(kT_e/m_e)^{1/2}$  and a positive ion flux that is typically (and  
 325 evidently in this case) much smaller. For the ambient Enceladus torus plasma ( $n_e \sim 100/\text{cm}^3$ ,  $T_e$   
 326  $\sim 3$  eV),  $F_e \sim 7 \times 10^9 / \text{cm}^2\text{-s}$ . For the dense plume plasma reported by Shafiq et al. (2011) for E3,  
 327  $n_e$  is perhaps  $10\times$  larger while  $T_e$  is perhaps of the same order of magnitude, resulting in a  $\sim 10\times$   
 328 enhancement of the electron thermal flux. Then the electron impact rate on a grain would be

329

330 
$$R_T = F_e S \sim (9 \times 10^{-4} / \text{s}) \left( \frac{a}{1 \text{ nm}} \right)^2 \quad (7a)$$

331

332 in the ambient torus plasma, or

333

334 
$$R_p = F_e S \sim (9 \times 10^{-3} / s) \left( \frac{a}{1 \text{ nm}} \right)^2 \quad (7b)$$

335

336 in the enhanced plume plasma.

337

338 The mean free path for a grain against electron impact is  $\lambda = v/R$  where  $v$  is the grain speed  
339 relative to Enceladus. As noted above,  $v$  is not measured, but we can put plausible limits on it. It  
340 is presumably at least of the order of the surface escape speed from Enceladus (240 m/s) or the  
341 grain would not have reached the point of observation  $\sim 1 R_E$  away. And it is presumably less  
342 than the flow speed of the neutral water vapor escaping the vents because the gas flow is  
343 presumably driving the grain flow, not vice-versa. By fitting a supersonic expansion model to  
344 the INMS gas density data from the three encounters analyzed here, Dong et al. (2011) obtain a  
345 gas flow speed in the range 500 – 800 m/s for all three encounters. Thus, assuming  $v \sim 500$  m/s  
346 for the grain speed, we obtain a mean free path  $\lambda$  for a grain of radius  $a$

347

348 
$$\lambda_T = v/R_T \sim (2 R_E) \left( \frac{1 \text{ nm}}{a} \right)^2 \quad (8a)$$

349

350 in the ambient torus plasma, or

351

352 
$$\lambda_p = v/R_p \sim (0.2 R_E) \left( \frac{1 \text{ nm}}{a} \right)^2 \quad (8b)$$

353  
354 in the enhanced plume plasma reported for E3. Thus, even in the ambient plasma environment,  
355 it is not unlikely that a nanograin will have acquired one excess electron within the distance of  
356 the E3 and E5 plume axis encounters (2.6 and 1.3  $R_E$  respectively), and it is quite likely in the  
357 enhanced plume plasma environment. It is even possible that the size dependence in (8) could  
358 explain the positive slope of the nanograin spectra in Figures 4 – 7 above. Smaller grains may  
359 well be present in greater numbers, but have had insufficient time to acquire even a single excess  
360 electron from the resident plasma.

361  
362 The existence of a relatively small but nonzero flux of positive nanograins on E3 and E5  
363 requires a different charging mechanism, of course. One possibility is that a small fraction of the  
364 impacting electrons have sufficient energy to liberate more than one secondary electron.  
365 Another possibility is the relatively small but nonzero flux of positive ions impacting the grains.  
366 A third possibility, as suggested by Jones et al. (2009), is triboelectric charging before escape.

367  
368 There is obviously much theoretical work to be done in quantitative modeling of the  
369 chemical and electrodynamic interactions between the nanograins and the plasma. For example,  
370 the thermal electron flux of the plume plasma is probably a strong function of distance from the  
371 source, because the plume plasma is probably created by impact ionization of the escaping water  
372 vapor, first by the ambient plasma and ultimately by the plume plasma itself in a bootstrap  
373 process. Nevertheless, the above simple calculation serves to illustrate that electron impact  
374 charging from the observed plasma is quite sufficient to explain the presence of (mostly

375 negative) charged nanograins in the plume. Additional encounter observations would be very  
376 helpful, of course.

377

### 378 **Timing difference between negative and positive grain signatures**

379

380 There is a clear and consistent timing difference between the sudden encounters with the  
381 negative and positive grain signatures on both E3 and E5; see Figures 2, 3, and 8. The negative  
382 (ELS) grain signature precedes the positive (IMS) grain signature on both encounters. The  
383 suddenness of the encounters is puzzling in itself. The timing of these encounters bears no  
384 obvious relationship to the encounter geometry – both are already well within the magnetic flux  
385 tube that would intersect Enceladus, assuming a north-south field orientation. Nor is there any  
386 obvious reason why that flux tube boundary would even matter to these high  $m/q$  particles that  
387 are not yet magnetically trapped. Moreover, the direction of the offset between negative and  
388 positive grain distributions is puzzling. It cannot be explained simply in terms of electrostatic  
389 deflection by the remnant corotation electric field, which has a positive radial component, and  
390 these are both inbound encounters. If the timing difference were produced by electric-field  
391 deflection, the positive grains should appear before the negative ones, not after as observed. We  
392 do not understand these encounter timing details, but we consider them worth mentioning as  
393 topics for future study.

394

395

395 **Conclusions**

396

397 During three ram-pointing encounters with the Enceladus south polar plumes, the Cassini  
398 Plasma Spectrometer has discovered and analyzed a new class of charged particles, nanometer-  
399 sized water ice grains. The  $E/q$  range of the CAPS detectors, coupled with the spacecraft  
400 encounter speeds, limits our detection to  $m/q$  values below  $\sim 10^4 - 10^5$  amu/ $e$  for the three  
401 available encounters, corresponding to  $\sim 1000 - 5000$  H<sub>2</sub>O molecular masses per elementary  
402 charge, but the resident particle distribution clearly extends to much higher  $m/q$  values that  
403 cannot be detected by CAPS.

404

405 We have argued that the most likely nonzero charge per grain is  $\pm 1 e$ , with negative grains  
406 outnumbering positive ones by a factor  $\sim 2000-3000$  within the CAPS  $E/q$  range, as required by  
407 the observations. We have also argued that this result is consistent with the idea that the  
408 nanograins leave Enceladus largely uncharged, and become increasingly negatively charged as  
409 they move away from Enceladus by attachment of electrons from the plume plasma. The  
410 nanograins are the primary carriers of negative charge away from Enceladus, and the implied  
411 electric current is evidently closed by the simultaneous escape of a dense plume plasma which  
412 has the opposite sign of (+) net charge density (Shafiq et al, 2011; Morooka et al., 2011). If this  
413 return current is not spatially coincident with the nanograin current, the implied current loop may  
414 have significant effects on the magnetic perturbations that have been observed on these and  
415 many other Enceladus encounters by the Cassini magnetometer (Khurana et al., 2007). In  
416 addition to the implied electric current system, there are many other remaining questions to be  
417 answered relating to the subsequent dynamics and resulting spatial distribution of the nanograins,

418 and their intimate coupling with the plasma and neutral gas. They undoubtedly make important  
419 contributions to the localized source of material for the Enceladus plasma torus and the E ring.

420

421 It is clear that we have much to learn about this novel phenomenon through further analysis  
422 of this data set and future close encounters of the Enceladus plume.

423

424 **Acknowledgments.** This work was supported in part by NASA JPL contracts 1243218 and  
425 1405851 to the Southwest Research Institute. Work at Los Alamos was conducted under the  
426 auspices of the U. S. Department of Energy, with support from NASA's Cassini project. Work  
427 at Mullard was supported by STFC (UK) and by ESA through the UK Science Agency. GHJ is  
428 supported by an STFC Advanced Fellowship. Work at Univ. Colorado was supported by the  
429 NASA Cassini Data Analysis Program. The RPWS-LP efforts are supported by the Swedish  
430 National Space Board (SNSB).

431

432

432 **References**

433

434 Coates, A. J., F. J. Crary, G. R. Lewis, D. T. Young, J. H. Waite Jr., and E. C. Sittler Jr. (2007),  
435 Discovery of heavy negative ions in Titan's ionosphere, *Geophys. Res. Lett.*, *34*, L22103,  
436 doi:10.1029/2007GL030978.

437

438 Coates, A. J., G. H. Jones, G. R. Lewis, A. Wellbrock, D. T. Young, F. J. Crary, R. E. Johnson,  
439 T. A. Cassidy, and T. W. Hill (2009), Negative ions in the Enceladus plume, *Icarus*,  
440 doi:10.1016/j.icarus.2009.07.013.

441

442 Coates, A. J., A. Wellbrock, G. R. Lewis, G. H. Jones, D. T. Young, F. J. Crary, J. H. Waite, R.  
443 E. Johnson, T. W. Hill, E. C. Sittler, Jr. (2010), Negative ions at Titan and Enceladus: recent  
444 results, *Faraday Discussions*, doi: 10.1039/C004700G2010.

445

446 Dong, Y., T. W. Hill, B. D. Teolis, B. A. Magee, and J. H. Waite (2011), The water vapor  
447 plumes of Enceladus, *J. Geophys. Res.*, doi:10.1029/2011JA016693, in press.

448

449 Farrell, W. M., W. S. Kurth, D. A. Gurnett, R. E. Johnson, M. L. Kaiser, J.-E. Wahlund, and J. H.  
450 Waite Jr. (2009), Electron density dropout near Enceladus in the context of water-vapor and  
451 water-ice, *Geophys. Res. Lett.*, *36*, L10203, doi:10.1029/2008GL037108.

452

453 Farrell, W. M., W. S. Kurth, R. L. Tokar, J.-E. Wahlund, D. A. Gurnett, Z. Wang, R. J.

454 MacDowall, M. W. Morooka, R. E. Johnson, and J. H. Waite Jr. (2010), Modification of the

455 plasma in the near-vicinity of Enceladus by the enveloping dust, *Geophys. Res. Lett.*, 37,  
456 L20202, doi:10.1029/2010GL044768.

457

458 Fraser, G. W. (2002), Ion detection efficiency of microchannel plates (MCPs), *Int. J. Mass Spec.*,  
459 215, 13-30.

460

461 Hansen, C. J., L. Esposito, A. I. F. Stewart, J. Colwell, A. Hendrix, W. Pryor, D. Shemansky,  
462 and R. West (2006), Enceladus' water vapor plume, *Science*, 311, 1422-1425.

463

464 Horányi, M. (1996), Charged dust dynamics in the solar system, *Ann. Rev. Astron. Astrophys.*,  
465 34, 383-418, doi:10.1146/annurev.astro.34.1.383.

466

467 Jones, G. H., and 20 others (2009), Fine jet structure of electrically charged grains in Enceladus's  
468 plume, *Geophys. Res. Lett.*, doi:10.1029/2009GL038284.

469

470 Khurana, K. K., M. K. Dougherty, C. T. Russell, and J. S. Leisner (2007), Mass loading of  
471 Saturn's magnetosphere near Enceladus, *J. Geophys. Res.*, 112, A08203,  
472 doi:10.1029/2006JA012110.

473

474 Mendis, D. A., and W. I. Axford (1974), The dynamics of micrometeoroids in planetary  
475 magnetospheres, *Ann. Rev. Earth Planet. Sci.*, 2, 419-430.

476

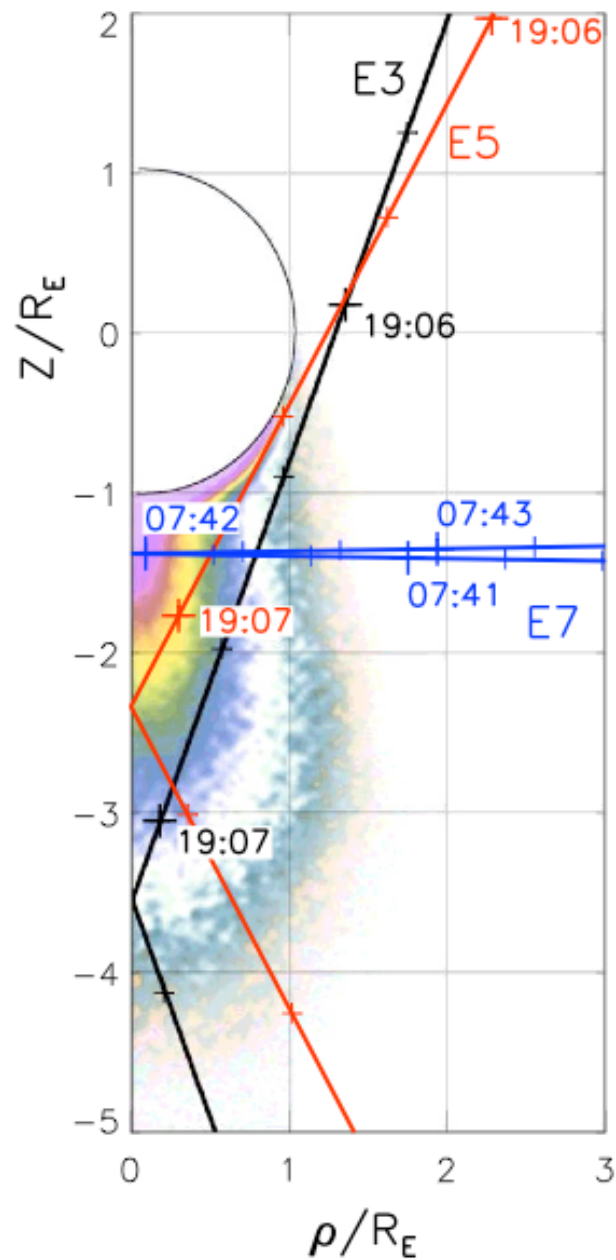
477 Morooka, M. W., J.-E. Wahlund, A. I. Eriksson, W. M. Farrell, D. A. Gurnett, W. S. Kurth, A.  
478 M. Persoon, M. Shafiq, M. André, and M. K. G. Holmberg (2011), Dusty plasma in the  
479 vicinity of Enceladus, *J. Geophys. Res.*, submitted.  
480  
481 Porco, C. C., and 24 others (2006), Cassini observes the active south pole of Enceladus, *Science*,  
482 *311*, 1393, doi:10.1126/science.1123013.  
483  
484 Shafiq, M., J.-E. Wahlund, M. W. Morooka, W. S. Kurth, and W. M. Farrell (2011),  
485 Characteristics of the dust-plasma interaction near Enceladus' south pole, *Plan. Space Sci.*,  
486 *59*, 17-25, doi:10.1016/j.pss.2010.10.006.  
487  
488 Smith, H. T., R. E. Johnson, M. E. Perry, D. G. Mitchell, R. L. McNutt, and D. T. Young (2010),  
489 Enceladus plume variability and the neutral gas densities in Saturn's magnetosphere, *J.*  
490 *Geophys. Res.*, *115*, A10252, doi: 10.1029/2009JA015184.  
491  
492 Spencer, J. R., J. C. Pearl, M. Segura, F. M. Flasar, A. Mamoutkine, P. Romani, B. J. Buratti, A.  
493 R. Hendrix, L. J. Spilker, and R. M. C. Lopes (2006), Cassini encounters Enceladus:  
494 background and the discovery of a south polar hot spot, *Science*, *311*, 1401-1405.  
495  
496 Tokar R. L., R. E. Johnson, M. F. Thomsen, R. J. Wilson, D. T. Young, F. J. Crary, A. J. Coates,  
497 G. H. Jones, and C. S. Paty (2009), Cassini detection of Enceladus' cold water-group plume  
498 ionosphere, *Geophys. Res. Lett.*, *36*, L13203, doi:10.1029/2009GL038923.  
499

500 Wahlund, J.-E., and 14 others (2009), Detection of dusty plasma near the E-ring of Saturn, *Plan.*  
501 *Space Sci.*, 57, 1795-1806, doi:10.1016/j.pss.2009.03.011.  
502

503 Waite, J. H. Jr., and 13 others (2006), Cassini Ion and Neutral Mass Spectrometer: Enceladus  
504 plume composition and structure, *Science*, 311, 1419-1422, doi:10.1126/science.1121290.  
505

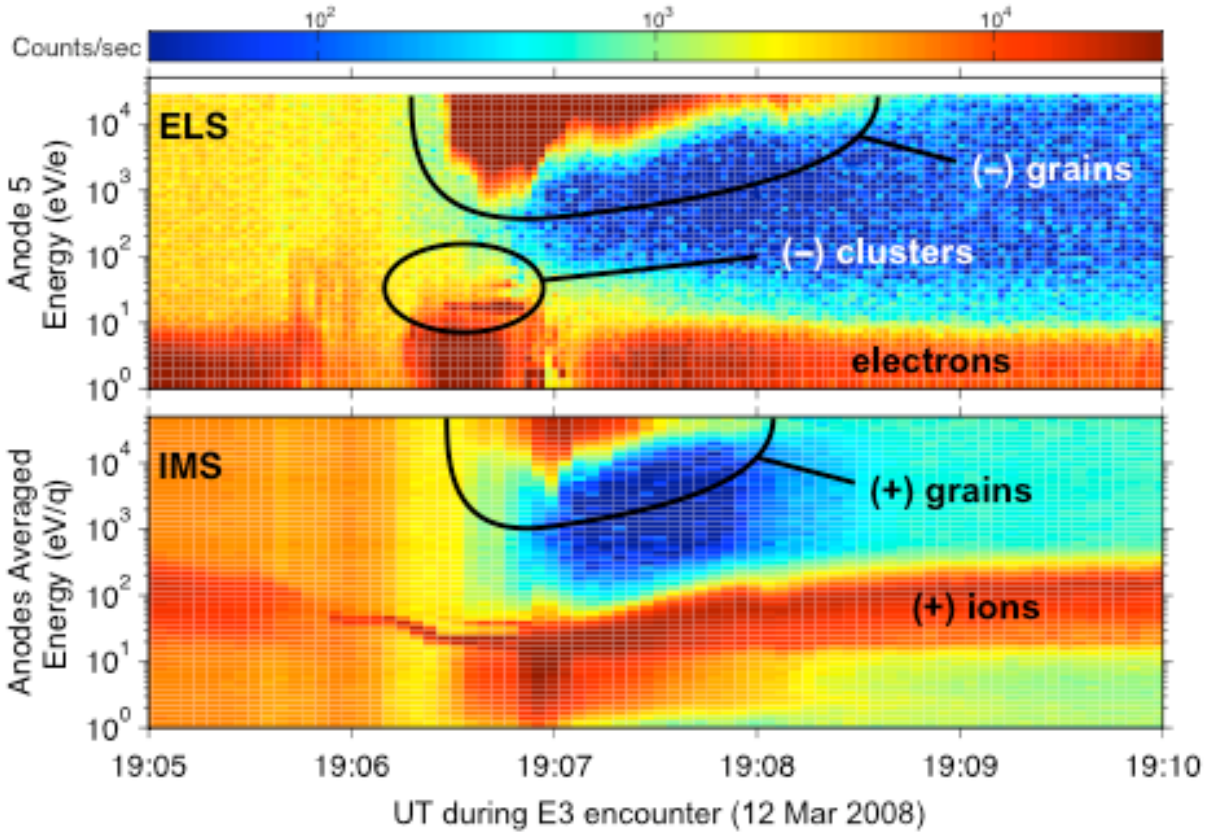
506 Waite, J. H. Jr., and 15 others (2009), Liquid water on Enceladus from observations of ammonia  
507 and <sup>40</sup>Ar in the plume, Supplementary Information, *Nature*, 460, 487-490,  
508 doi:10.1038/nature08153.  
509

510 Young, D. T., and 57 others (2004), Cassini Plasma Spectrometer investigation, *Space Sci. Rev.*,  
511 114, 1.  
512



513

514 Figure 1. The three Cassini Enceladus plume encounters to date that have had CAPS ram  
 515 pointing, in a  $(\rho, z)$  cylindrical coordinate system aligned with the polar axis of Enceladus. Times  
 516 (UT) are marked at 20-sec intervals and labeled at 1-min intervals. The background color is a  
 517 depiction of the intensity of the visible dust signal detected by the Cassini Imaging Science  
 518 Subsystem (<http://saturn.jpl.nasa.gov/photos/imagetdetails/index.cfm?imageId=2985>).



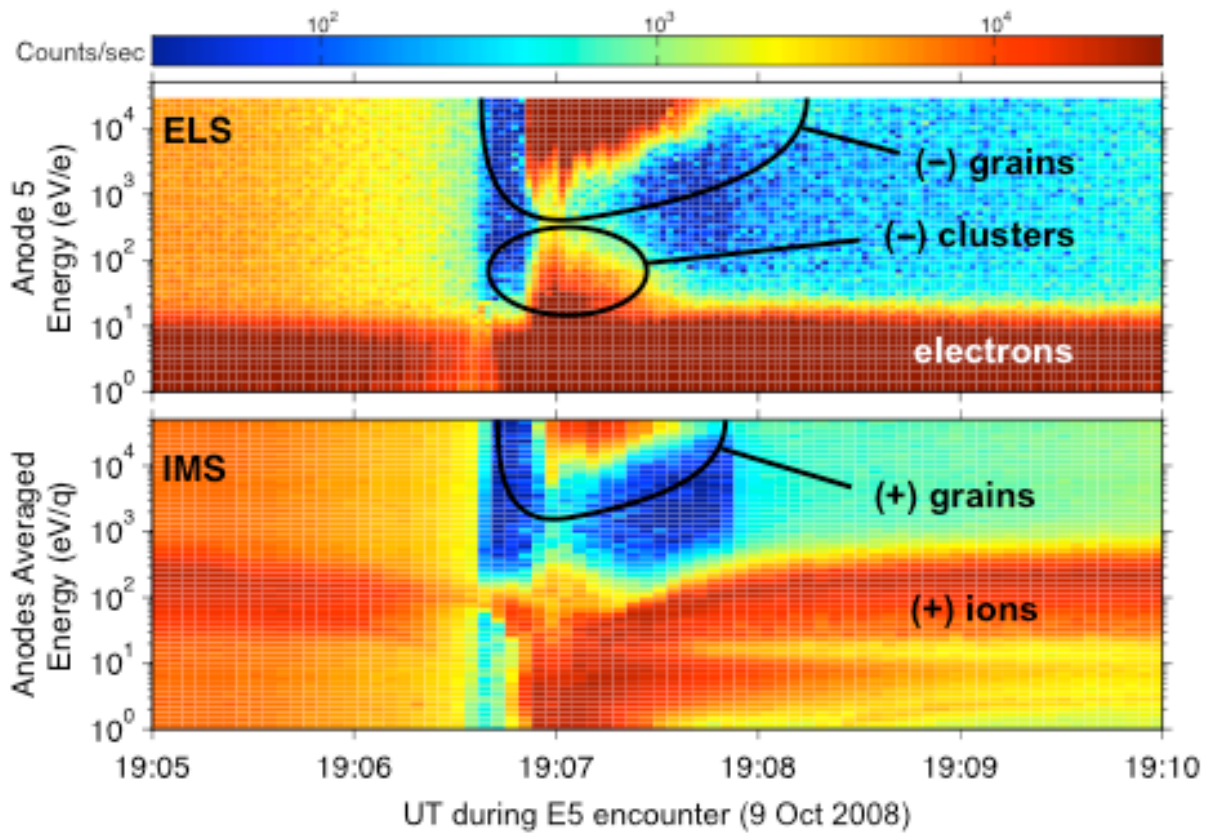
519

520

521 Figure 2. CAPS counting-rate spectrograms for the E3 Cassini encounter on 12 Mar 2008. The  
 522 grain signatures at the highest energies are the subject of this paper. The diffuse background is  
 523 due to penetrating energetic particles, which largely disappear during passage through the  
 524 satellite's corotational wake.

525

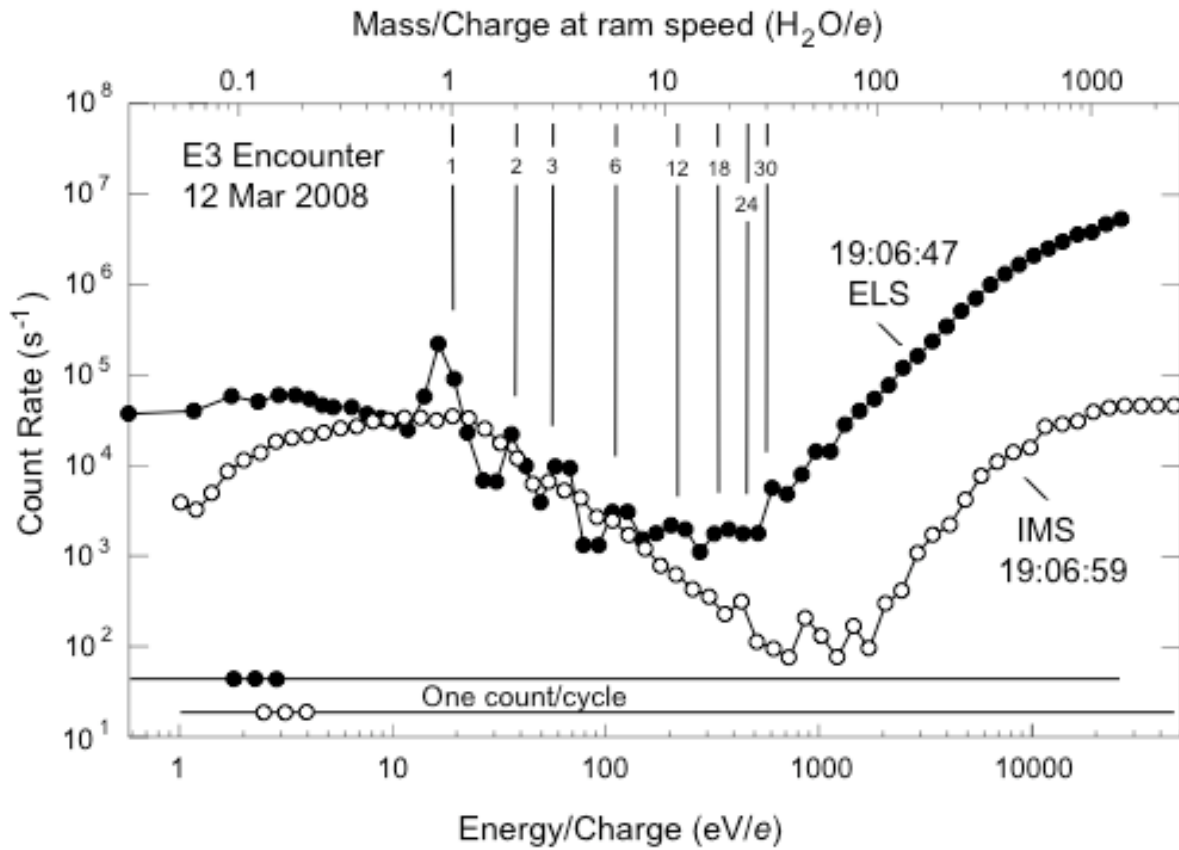
526



527

528 Figure 3. Same as Figure 2, but for the E5 encounter on 9 Oct 2008.

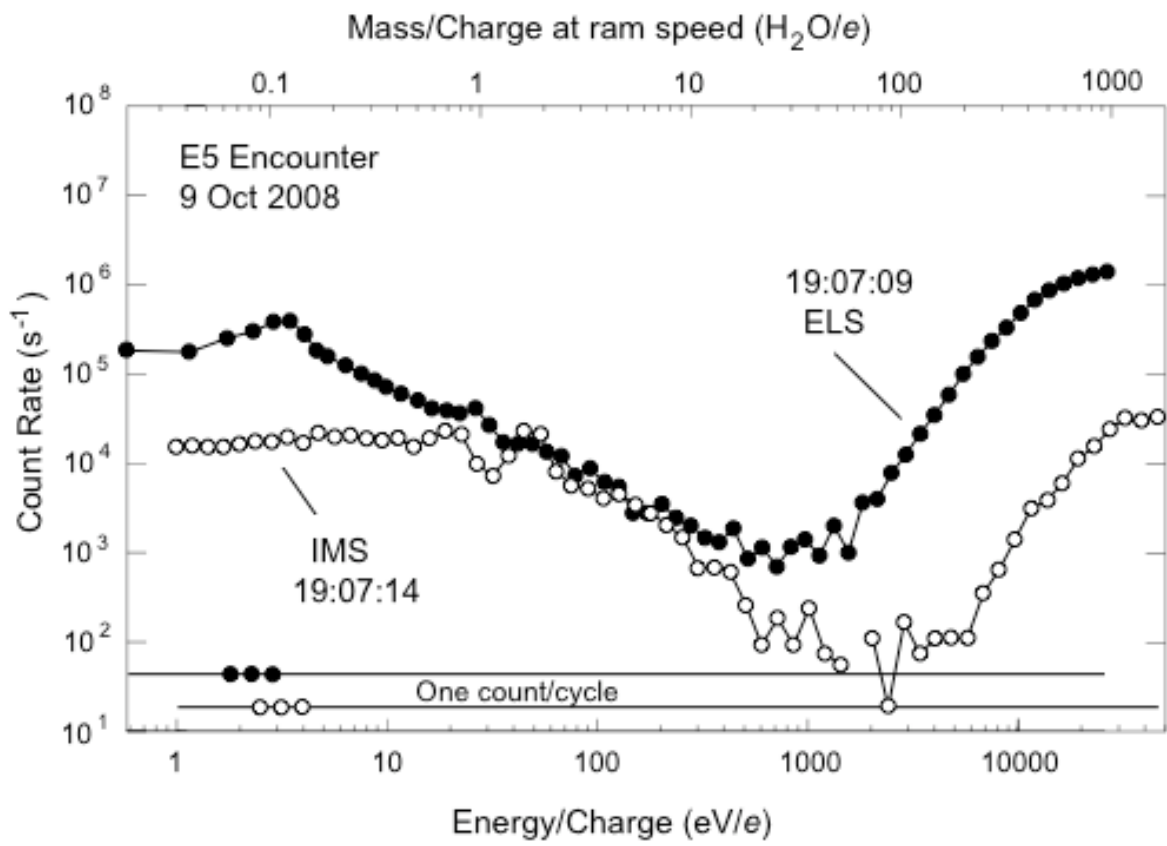
529



529

530 Figure 4. Counting rate spectra for negative (ELS) and positive (IMS) charged particles during  
 531 the E3 encounter near the peak of the nanograin flux. The observed  $E/q$  range (bottom  
 532 horizontal scale) is converted to  $m/q$  at the ram speed on the top horizontal scale, in units of  
 533 water molecular masses per elementary charge.

534

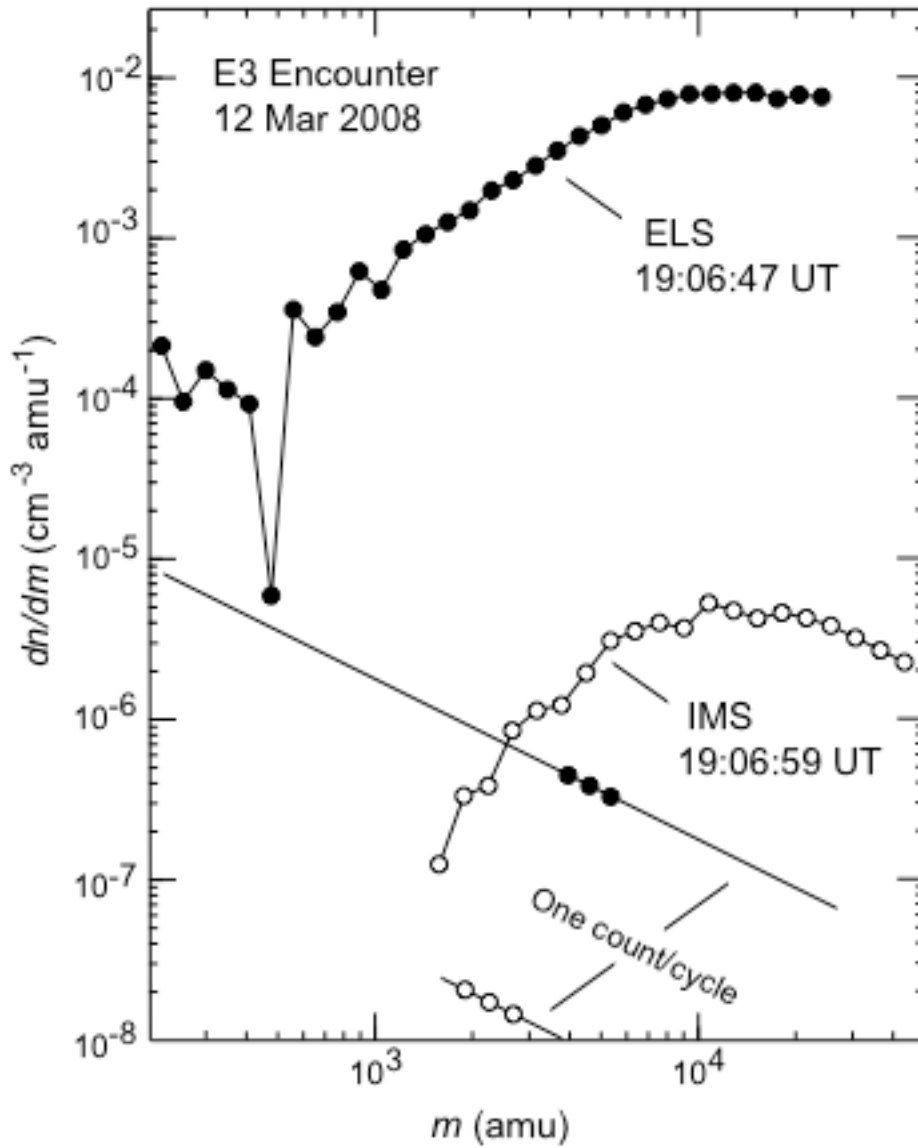


534

535

536 Figure 5. Same as Figure 4, for the E5 encounter.

537



537

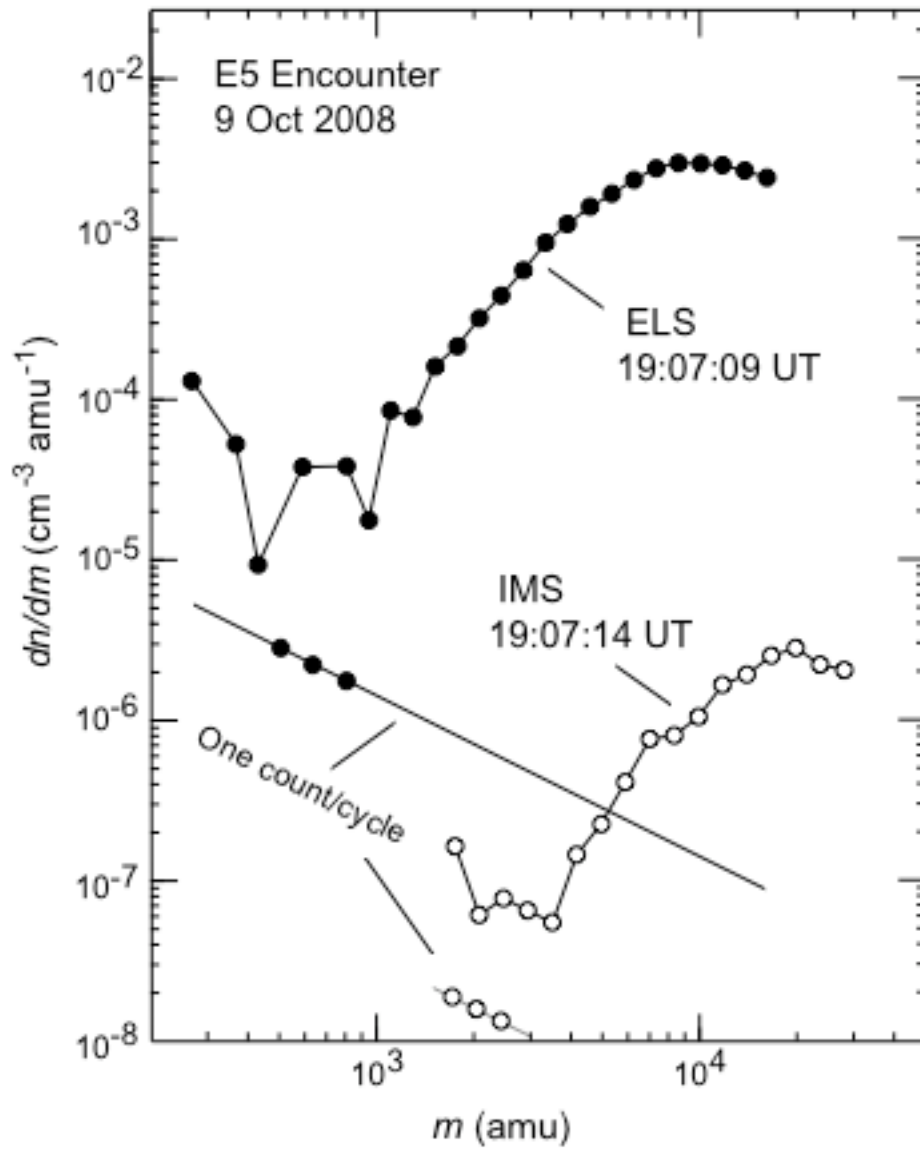
538

539 Figure 6. Charged nanograin number density per unit mass obtained from equation (1) with ELS

540 and IMS counting rates near the times of the peak nanograin fluxes on the E3 encounter.

541

542



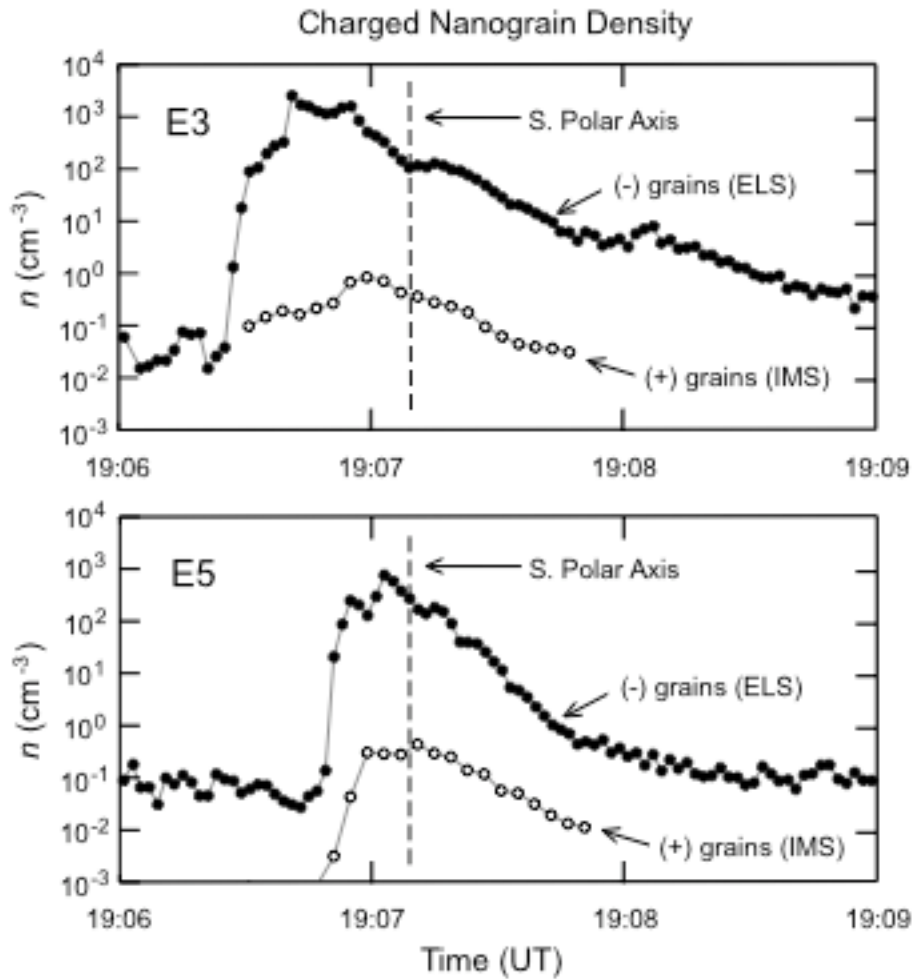
542

543

544 Figure 7. Same as Figure 6 for the E5 encounter.

545

546



546

547

548 Figure 8. Total number densities of nanograins within the CAPS  $E/q$  (or  $m/q$ ) ranges versus time

549 during the E3 (top) and E5 (bottom) encounters. At each time step, the total density is obtained

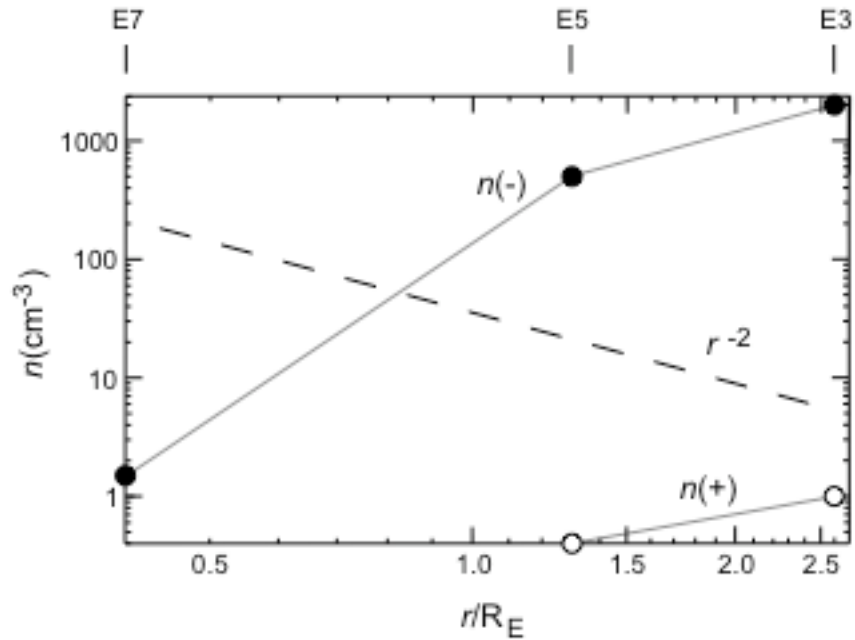
550 by integrating over  $dn/dm$  spectra like those shown in Figures 6 and 7. The vertical dashed line

551 shows the time of the closest approach to the south polar axis of Enceladus, which occurred (by

552 coincidence) at 19:07:09 UT for both encounters.

553

554



554

555

556 Figure 9. Maximum observed values of negatively and positively charged nanograin number  
 557 density within the CAPS energy range observed during the three encounters analyzed here. The  
 558 abscissa is distance from the south pole on the surface of Enceladus, not from the center of  
 559 Enceladus. The nominal (flux-conserving)  $1/r^2$  dependence is shown by the dashed line for  
 560 comparison.

561